Nanoscale

Accepted Manuscript

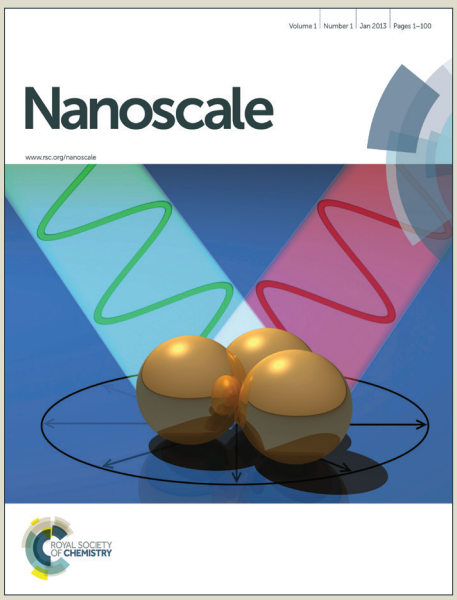

ROYAL SOCIETY OF CHEMISTRY

www.rsc.org/nanoscale

First-time Electrical Characterization of Nanotubular ZrO_2 Films for Micro-Solid Oxide Fuel Cell Applications

Aligul Buyukaksoy[1], Tobias Fürstenhaupt[2] and Viola I. Birss[1]*

1 Department of Chemistry, University of Calgary, Calgary, Alberta, Canada, T2N 1N4

2 Microscopy and Imaging Facility, University of Calgary, Canada, Alberta T2N 4N1

* Corresponding author contact information: Tel.: +1 (403) 220-7306 Fax: +1 (403) 289-9488
E-mail: birss@ucalgary.ca

Abstract

In this work, anodically grown ZrO_2 nanotubes (NTs) are examined for the first time for use in micro solid oxide fuel cell (μ-SOFC) applications. This is due to their high surface area to volume ratio and useful nanoscale morphological features (e.g., 5-100 nm thick NT bases that could serve as the electrolyte layer). To understand their full potential for these applications, the determination of their electrical properties is necessary. Therefore, ZrO_2 NTs, in the form of a uniform and crack-free film, were obtained by the two-step anodization of Zr foil in aqueous solutions. The films exhibited excellent adhesion to the Zr substrate, which facilitated impedance spectroscopy analyses, used for the first time to obtain the resistivity of the nanotubular array separately from the contact resistances. This gave a conductivity of the ZrO_2 NTs of 1.6×10^{-6} S/cm at 600 ℃ in N_2, approximately twice that reported for dense ZrO_2 films measured at the same temperature in air, and also a very reasonable activation energy of 0.90 eV in the 400-600 ℃ temperature range.

Keywords: ZrO_2 nanotubes, solid oxide fuel cells, electrical conductivity, impedance spectroscopy, anodization

Introduction

Anodically grown nanotubular metal oxide structures have gained wide interest in various applications, primarily due to their high surface area to volume ratio, ordered unidirectional morphology, and the tunability of their structural properties (e.g., tube length, pore size, wall thickness, etc.) [1-3]. Of the valve metal oxides, anodized TiO_2 has been the focus of the majority of the investigations [4-8], mainly due to its direct applicability in photocatalysis. The high surface area and stability provided by nanotubular TiO_2 structures was reported to be highly beneficial to boosting their photocatalytic activity [4, 5].

ZrO_2 is another valve metal oxide that can be grown anodically in the form of nanotubes (NTs), although only a few examples have been reported to date [9, 10]. This is due primarily to the relatively limited applicability of this material in current devices. However, in the Y_2O_3 or CaO-doped form, ZrO_2 becomes an ionic conductor with negligible electronic conductivity at high temperatures, which makes ZrO_2 of great interest as an electrolyte for solid oxide fuel cells (SOFCs) [11-13] and solid state-gas sensors [14].

Although SOFC electrolytes are normally composed of Y_2O_3-stabilized ZrO_2 (YSZ), it was reported recently [15] that micro solid oxide fuel cells (μ-SOFCs), based on a < 50 nm thick undoped ZrO_2 thin film electrolyte, could be viable. This μ-SOFC demonstrated a relatively high open circuit potential (OCP) of ~0.91 V at 450 ℃ (vs. the theoretical OCP of 1.10 V at 450 ℃) [15]. The maximum power density of 30 mWatt/cm^2 obtained at this low temperature was in the range of what is reported for μ-SOFCs utilizing YSZ electrolytes, which is also quite encouraging. These results suggest that the main requirements for a viable μ-SOFC electrolyte,

namely a high OCP and low resistance, can be met by undoped ZrO_2 as long as it is sufficiently thin, i.e., < 50 nm.

In the light of this development, anodically grown nanotubular ZrO_2 structures may be promising materials for μ-SOFC applications. In conventional μ-SOFCs, the electrode/electrolyte interface consists of a 50-400 nm thick doped ZrO_2 electrolyte and a porous electrocatalyst thin film, with the porosity serving to generate a high triple phase boundary (TPB) length where the electrocatalytic reactions take place (Figure 1a). On the other hand, the deposition of porous electrocatalyst materials into the ZrO_2 NTs would allow the base of the ZrO_2 NT to serve as the electrolyte (5-50 nm thickness), while also increasing the TPB length (electrocatalyst/ZrO_2 interfacial area) along the NT walls (Figure 1b). In this way, a significantly enhanced TPB length per unit geometric electrode area (and hence a significantly enhanced power density), in comparison to the reported value in Ref [15], should be obtainable. This μ-SOFC design is similar in some ways to a recently reported system, in which a high TPB length was achieved by depositing a thin layer of ZrO_2 via atomic layer deposition on the surface of Ni nanowires, followed by cathode layer deposition on the zirconia surface [16].

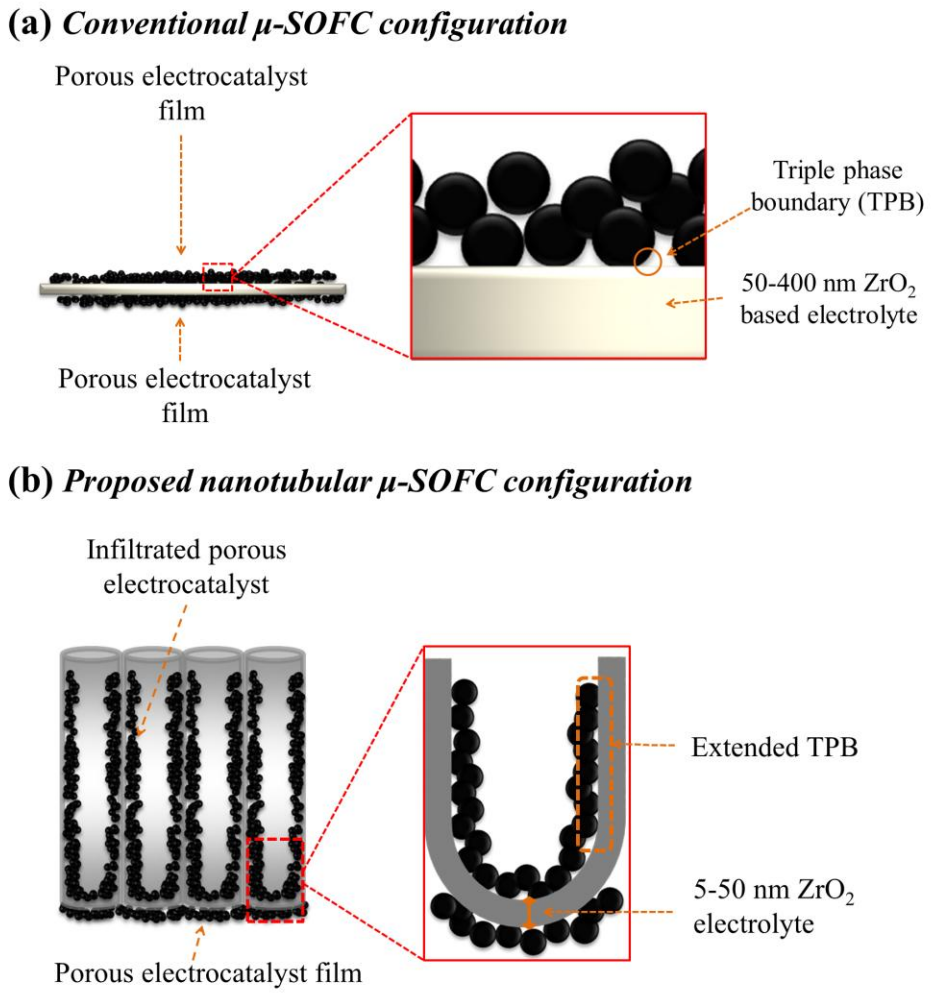

Figure 1. Schematic representation of (a) conventional μ-SOFC and b) proposed nanotubular μ-SOFC, showing thinner electrolyte and higher triple phase boundary length than in (a).

In order to realize the full potential of ZrO_2 NTs for use in μ-SOFCs, however, their electrical conductivity must be determined. It has been frequently observed that, during anodization, islands of NT bundles form, which makes it challenging to obtain stable electrical contacts and accurate electrical conductivity results [17-20]. Thus, in the present study, a two-step anodization method was used to produce a continuous film of ZrO_2 NTs without island (bundle) formation. The electrical conductivity of the NTs was determined by impedance

spectroscopy, which allowed us to distinguish the contributions from charge conduction in the ZrO_2 NTs from the contact resistance of the current collectors to the NTs, an issue which has not been addressed in prior attempts to measure the electrical conductivity of other NTs, e.g., TiO_2 [21]. It is also shown here that the electrical conductivity of the ZrO_2 NTs is higher than expected, making the ZrO_2 NTs a highly promising candidate for μ-SOFC applications.

Experimental Methods

ZrO_2 Nanotube Fabrication

Metallic Zr substrates were cut from as-received Zr foil (Alfa Aesar, 0.25 mm thick, 99.95% purity) and then rinsed sequentially with acetone, isopropanol and methanol. A two-electrode setup with a Pt gauze cylinder counter electrode was used for the anodization of the Zr substrates. A two-step anodization was performed to obtain nanotubular ZrO_2 films of different tube lengths.

To construct the nanotubular films, the first step involved anodization for 30 minutes at 20 V vs. a Pt counter electrode in a 1 M $(NH_4)_2SO_4$ solution, containing 4.5 wt% NH_4F (Princeton Applied Research 263A potentiostat). After the oxide films were dried in air, they were peeled away from the Zr substrate, exposing a now shiny Zr surface. A second anodization step was carried out for 5 minutes in a 1 M $(NH_4)_2SO_4$ solution, containing 0.5 wt% NH_4F, at voltages ranging from 10 to 20 V to obtain NTs with varying thicknesses. However, for the sake of clear comparison, only NTs fabricated by performing a second anodization step at 10 and 20 V will be discussed here.

Electrical Characterization

The electrical conductivity measurements of the ZrO_2 nanotubular films were performed by impedance spectroscopy (Solatron ECS Modulab), using a four-lead two-probe configuration. A segment of the Zr substrate was kept free of NTs by keeping it out of the anodization solution during NT formation. This was subsequently covered with Ag paste to serve as the electrical contact at the base of the nanotubular film, while the other electrical contact (on the top surface of the NTs) was also achieved using Ag paste (Figure 2). Ag wires were then attached to the Ag paste to serve as lead wires for both contacts. The conductivity measurements were carried out at 250-600 ℃, under N_2 flow, mainly to avoid the oxidation of the Zr substrate in air and hence an increase in the total resistance, and also to avoid embrittlement-induced cracking of Zr in hydrogen environments, a well-known phenomenon in the literature [22, 23].

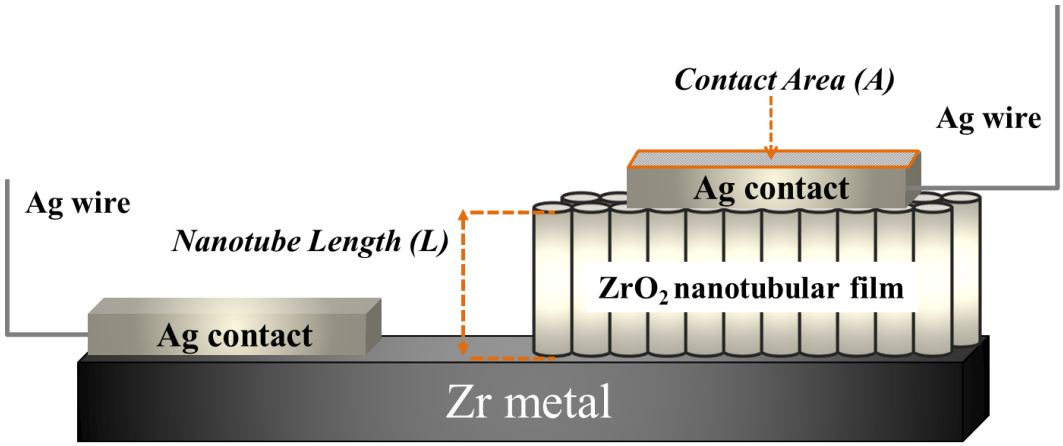

Figure 2. Schematic representation of the experimental setup used for the electrical conductivity measurements of the nanotubular ZrO_2 films.

Morphological Characterization

Morphological characterization of the ZrO_2 nanotubular films was performed using a field emission scanning electron microscope (FE-SEM, SEM, Carl Zeiss Sigma, University of Calgary). All Transmission Electron Microscopy (TEM) work was carried out on a Tecnai TF20 G2 FE-TEM (FEI, Hillsboro, Oregon, USA) at a 200 kV accelerating voltage with a FEI double tilt low background holder (Type PW6595/15). The TEM brightfield images were captured on a Gatan UltraScan 4000 CCD (Gatan, Pleasanton, California, USA) at 2048x2048 pixels. Energy-dispersive X-ray spectroscopy (EDX) was performed with a CM-20T detector from EDAX, Mahwah, NJ, USA. Live time was about 500 s and the beam intensity was adjusted to give a dead time between 20% and 40%.

To remove the oxide layer formed by the first anodization step, the anodized samples were immersed in ethanol and sonicated for two hours. This caused the ZrO_2 NTs to detach from the underlying Zr foil and become suspended in the ethanol. A single droplet of this suspension was placed on one side of a standard TEM Grid that was covered with a ~40 nm thick holey carbon film (EMS, Hatfield, Pennsylvania, USA) and left to dry for several minutes in air.

Results and Discussion

Morphological Characterization

FE-SEM analysis of the Zr surface after the first anodization step, which was performed in an aqueous 1 M $(NH_4)_2SO_4$ + 5 wt% NH_4F solution for 30 minutes at 20 V, reveals a rough oxide surface morphology (Figure 3a). The oxide layer was peeled away from the Zr surface by slightly bending the Zr metal foil and allowing the oxide layer to delaminate. The base of this

oxide layer was then examined. Highly ordered, inverted spherical caps with an average diameter of ca. 70 nm are observed (Figure 3a inset). Figure 3b shows the SEM image of the shiny Zr surface, obtained after the oxide layer formed in the first anodization step was removed. A uniform surface, consisting of dimples with a diameter of ca. 70 nm, is observed (Figure 3b). These dimples have been seen at the surface of other valve metals after the removal of anodically formed oxide films (e.g., at Ta and Ti [20, 24-27]), where the dimples at the surface were reported to be the imprints of the spherical caps observed at the base of the oxide layer (Figure 3a inset). The formation of dimples after the first anodization step argues that, although the oxide film exhibits an irregular outer surface morphology, it has an ordered nanotubular structure near the Zr substrate.

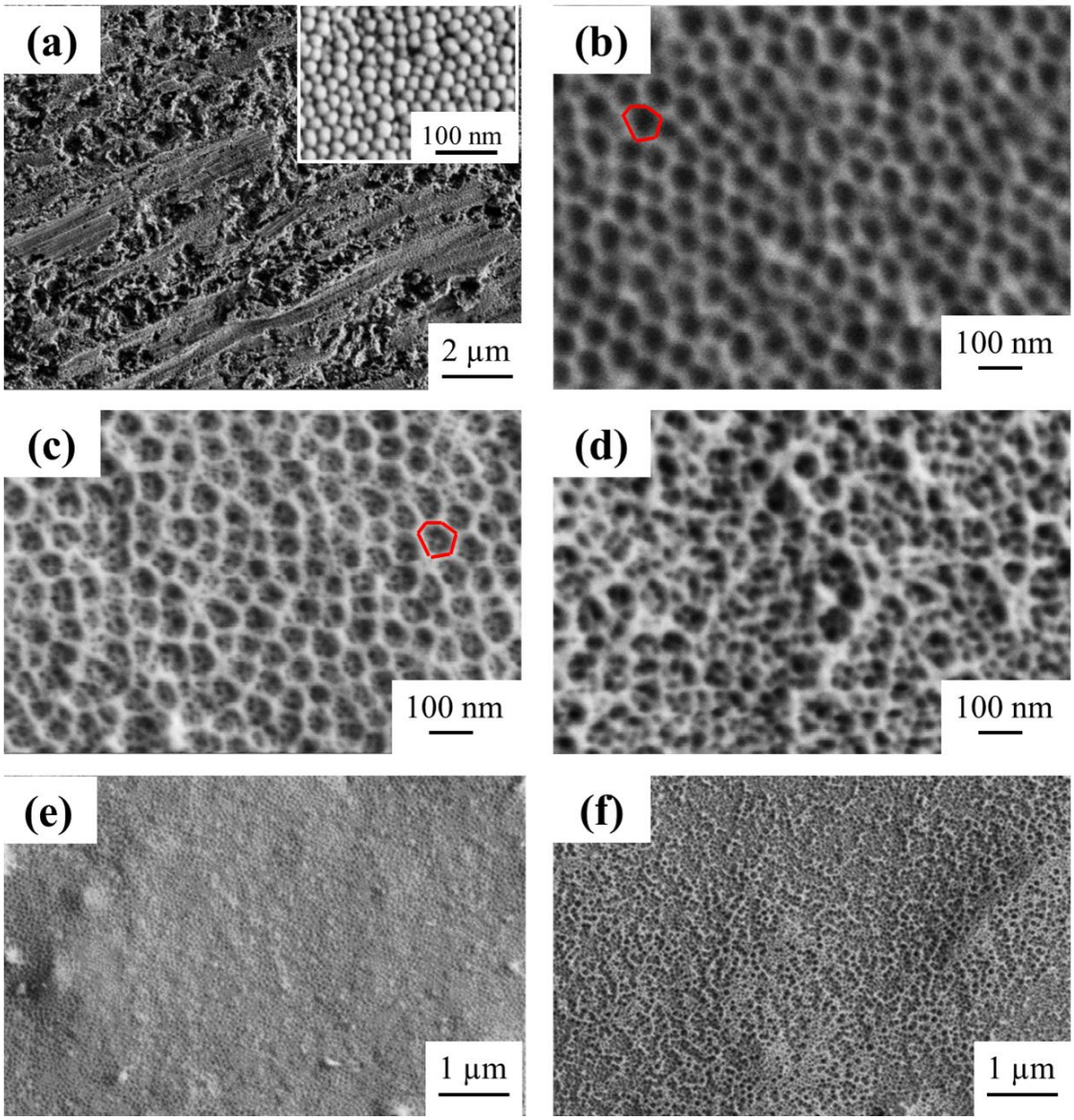

Figure 3. FE-SEM images of the Zr foil surface (a) after the first anodization step carried out at 20 V, with the base of the oxide layer (removed from the Zr surface) shown in the inset, (b) the Zr surface after the first anodized oxide layer was removed, and the ZrO_2 nanotubular film obtained by a second anodization step (c) at 10 V and (d) at 20 V, with lower magnification FE-SEM images of (c) and (d), shown in (e) and (f), respectively.

Shorter NTs were fabricated by carrying out a second anodization step on the dimpled Zr surface, using an anodization voltage of 10 V for 5 minutes in a similar solution as used for the

first anodization step, but with a lower NH_4F content (0.5 wt%). A two-layered morphology of the oxide layer is seen in Figure 3c. The outermost layer consists of a honeycomb-structured surface film containing ~70 nm pores and ~5 nm wide pore walls, while the layer beneath this surface film consists of NTs ~15 nm in inner diameter. It is noted that the honeycomb-shaped outer layer is the exact replica of the dimples formed in the first anodization step (Figure 3b).

The second anodization step results in the formation of a nanotubular film that lifts the honeycomb-shaped layer. The smaller pore size of the underlying nanotubular film is due to the lower anodization voltage used (10 V) in comparison with the first anodization step (20 V) [1, 4]. Although a similar honeycomb-like surface film has been reported recently for TiO_2, to the best of our knowledge, it is being reported for the first time here for ZrO_2 [27-29]. It is also worth mentioning that, due to the highly porous nature of this outer layer, it should not impede gas transport inside the underlying NTs or hamper electrocatalyst infiltration to form the μ-SOFC electrodes, as proposed in Figure 1b.

Fabrication of the thickest nanotubular film was achieved by performing a second anodization step on the dimpled Zr surface, using an anodization voltage of 20 V for 5 minutes in a solution identical to that used in the second anodization step to make the shorter NTs (Figure 3d). The thin, honeycomb-structured surface film, seen for the shorter NTs, is not observed for the longer NTs. On the other hand, a surface structure that appears to contain broken pieces of the honeycomb-like layer is visible (Figure 3d). It is suggested that the honeycomb-structured surface layer existed in the earlier stages of the second anodization step, but was damaged as a result of the second anodization step carried out at 20 V. The anodization voltage of 20 V, used

in the first and the second steps to fabricate longer NTs, forms dimples and NTs having the same diameter, which must strain the overlying honeycomb-like surface layer and break it apart.

It has been observed repeatedly in the literature that NTs grown by anodization form irregular patches or bundles of NTs [17-20]. However, to be able to perform accurate electrical measurements of the ZrO_2 NTs, a crack-free and continuous film of ZrO_2 NTs, which adheres well to the Zr metal substrate, is required. It has been reported for Ti [27-29] that a two-step anodization resulted in crack-free, continuous TiO_2 films. The low magnification images of the shorter and longer ZrO_2 NTs in Figure 3e and 3f also formed in the present work in two steps, confirming that the films are continuous and free of cracks. It is also worth mentioning that, due to the significantly lower NH_4F concentration used in the second anodization step, the oxide films adhere strongly to the Zr substrate.

More detailed morphological information was obtained by the TEM analysis of the nanotubular structures (Figure 4). A typical example of shorter NTs is given in low (Figure 4a) and high magnification (Figure 4b) bright field TEM images. The shorter NTs are ca. 2 μm in length with an average internal diameter of 15 nm and an average wall thickness of 8 nm, while the longer NTs formed at 20 V are ca. 5 μm in length with an average internal diameter of 22 nm and a wall thickness of 30 nm (Figures 4d and e). It is also evident from the high magnification TEM images (Figures 4d and e) that the thickness of the NT bases is almost identical to the wall thickness. The EDX spectrum obtained from both of these NTs shows the presence of fluoride in the nanotubular structures (Figures 4c and 4f), which originates from anodization in the fluoride-containing solutions. Additionally, electron energy loss spectroscopy (EELS) measurements were carried out, further confirming the presence of 1-3 at. % fluoride (results not shown here),

while the Cu signal in the EDX spectrum originates from the Cu TEM grid. A summary of the morphological parameters of both the shortest and longest NTs, along with the nanotubular ZrO_2 film porosity, determined from the ratio of the cylindrical pore volume in a single NT to its pore-free cylindrical volume, is given in Table I.

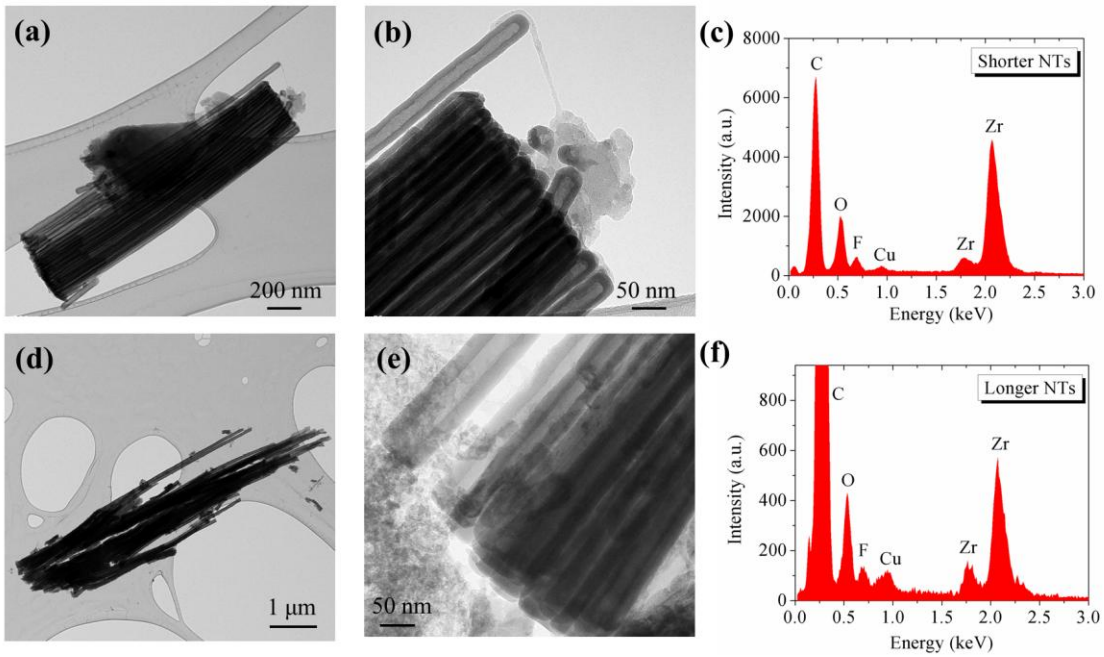

Figure 4. (a) Low and (b) higher magnification bright field TEM images of 2 µm long ZrO_2 NTs and (c) the corresponding EDX spectrum. (d) Low magnification and (e) high magnification bright field TEM images of 5 µm long ZrO_2 NTs and (f) the corresponding EDX spectrum.

Table I. Summary of morphological parameters of shortest and longest ZrO_2 NTs. Five measurements from four different specimens was taken to obtain these parameters.

Nanotube length (µm)	**Nanotube inner diameter (nm)**	**Nanotube Wall thickness (nm)**	**Nanotube Base thickness (nm)**	**Nanotubular ZrO_2 film porosity (%)**
2.0 ±0.3	7.9 ±0.8	15.1 ±1.7	15.3 ±1.2	16
5.1 ±0.4	22.0 ±2.3	30.2 ±2.3	29.6 ±2.1	22

As explained above, the ZrO_2 nanotubular films developed here are being considered for μ-SOFC applications (Figure 1b). Thus, morphological stability at operating temperatures (400-600 ℃) is essential. For this reason, the ZrO_2 nanotubular films (shorter NTs) were annealed at 600 ℃, the upper limit of μ-SOFC operation, for 8 hours in N_2. The SEM analysis shows that the nanotubular structure is retained even after this annealing process is complete (Figure 5). It has been reported that ZrO_2 NTs undergo significant morphological changes when heat-treated at temperatures > 600 ℃ due to changes in their crystal structure, but retain their nanotubular structure at lower temperatures [30, 31]. Therefore, the morphological stability, observed in this work at 600 ℃, is in good agreement with prior literature [30, 31].

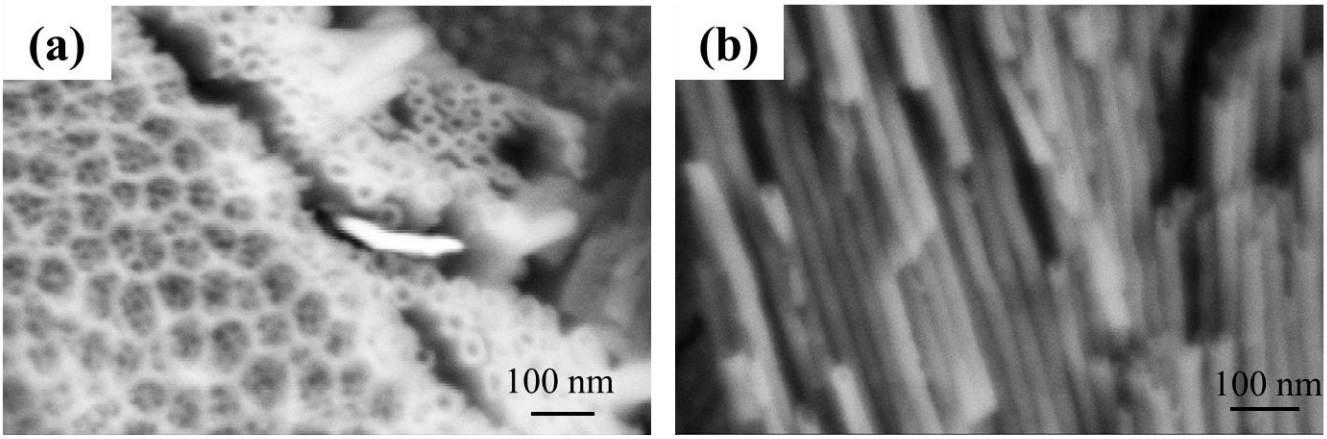

Figure 5. FE-SEM image of 2 μm thick ZrO_2 nanotubular film showing (a) top-down surface and (b) cross-sectional views after annealing in N_2 at 600 ℃ for 8 hours.

Electrical Characterization

For ZrO_2 nanotubular films to be of use in SOFC applications, knowledge of their electrical conductivity is critical in order to predict the power output. The higher the resistance of the electrolyte, the less power can be generated. To date, efforts to measure the electrical

conductivity of oxide NTs have been very limited. For example, the electrical conductivity of TiO_2 nanotubular films was investigated by current-voltage measurements using a similar setup as shown in Figure 2 [21]. However, in another study, it was shown that the measured resistance, obtained from oxide films deposited on metallic substrates, includes a significant contribution from the oxide film/contact interface [32]. Therefore, impedance spectroscopy, which has been used to identify the individual resistance contributions in bulk oxide ceramics [33, 34], was used here to determine the electrical conductivity of the ZrO_2 nanotubular films (Figures 3c-e and Figure 5) after annealing in air at 600 ℃ for 8 hours.

Figure 6 shows a typical impedance spectrum obtained from the 2 μm thick ZrO_2 nanotubular film and the equivalent circuit model used to perform the data fitting. Two units in series, each consisting of a resistor in parallel with a constant phase element (CPE), were selected to fit the impedance spectrum. Excellent fittings, with χ^2 values in the 10^{-4}-10^{-5} range, were obtained. R1-CPE1 defines the high frequency time constant and corresponds to the resistance of the ZrO_2 nanotubular film itself, while the low frequency semicircle is defined by the R2-CPE2 element. It is well-known that charge transfer processes at the electrode/current collector interfaces are much slower than electrical conduction within ZrO_2 [35]. Therefore, the low frequency semicircle is ascribed to the contact at the Ag/ZrO_2 and Zr/ZrO_2 interfaces (Figure 2). Accordingly, only the high frequency semicircle, defined by the R1-CPE1 element, was then used to calculate the electrical conductivity of the ZrO_2 NTs.

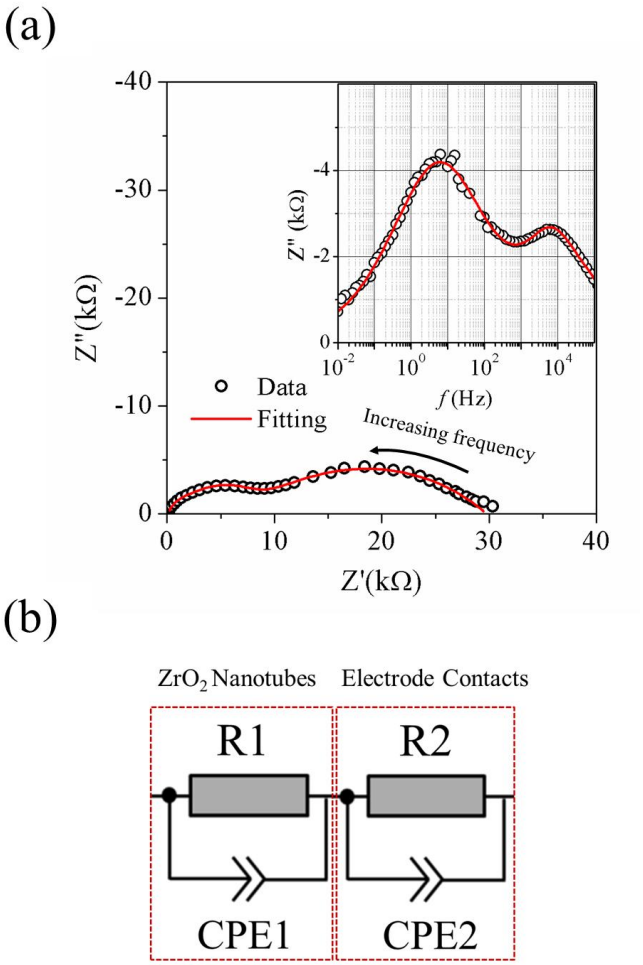

Figure 6. Representative impedance spectra for the 2 μm long NTs represented by both Nyquist and Bode (inset) plots, showing two relaxation time constants, with the corresponding fitting shown in (a), while (b) shows the equivalent circuit diagram used to perform the fitting.

To validate the choice of the equivalent circuit shown in Figure 6b and the physical meanings ascribed to the R-CPE elements, the impedance spectra obtained from NTs of variable length were compared. As mentioned earlier (Table I), the length of the shortest NTs is ca. 2 μm and the length of longest NTs is ca. 5 μm. According to the equivalent circuit model shown in Figure 6, and assuming that the both shortest and longest ZrO_2 NTs have the same intrinsic resistivity, the high frequency semi-circle, which was ascribed to the ZrO_2 NT resistance, should

increase approximately 2.5 times for the longest versus shortest NTs, while the semicircle related to the electrode contact resistance should remain unaffected by the increase in the nanotubular film thickness.

Figure 7 compares the impedance spectra obtained at 600 ℃ in N_2, with a change in the spectrum with increased NT length clearly seen. The inset in Figure 7a shows the high frequency part of the impedance response, revealing a significant increase in the resistance. The R_{ZrO2} and $R_{contact}$ values, extracted from the impedance data using the equivalent circuit in Figure 6b, are given in Table II. Evidently, the R_{ZrO2} value varies significantly with NT length, while the $R_{contact}$ value remains unchanged.

Table II. R_{ZrO2} and $R_{contact}$ values extracted from equivalent circuit fitting of the impedance data for ZrO_2 NTs at 600 ℃ in N_2.

Nanotube length (μm)	**R_{ZrO2} ($k\Omega.cm^2$) ***	**Fitting Error (%)**	**$R_{contact}$ ($k\Omega.cm^2$) ***	**Fitting Error (%)**
2.0 ±0.3	2.1	3.8	27.5	8.5
5.1 ±0.4	4.2	4.5	28.5	7.8

* R_{ZrO2} refers to the resistance of the ZrO_2 nanotubular films, while $R_{contact}$ refers to the resistance at the Ag/ZrO_2 and Zr/ZrO_2 contact interfaces.

The change in the normalized R_{ZrO2} and $R_{contact}$ values with normalized NT length is given in Figures 7b and 7c. It is seen that a 2.5 times increase in the NT length results in a 2.1 times increase in the R_{ZrO2} values (Figure 7b), while no significant change in the electrode contact resistance is observed. This validates the choice of the equivalent circuit employed in Figure 6, as well as the physical meaning of the R-CPE elements. The slightly smaller increase in R_{ZrO2}

than expected is likely due to the small differences in the porosity of the nanotubular films, as well as due to fitting and NT length measurement errors (Table II).

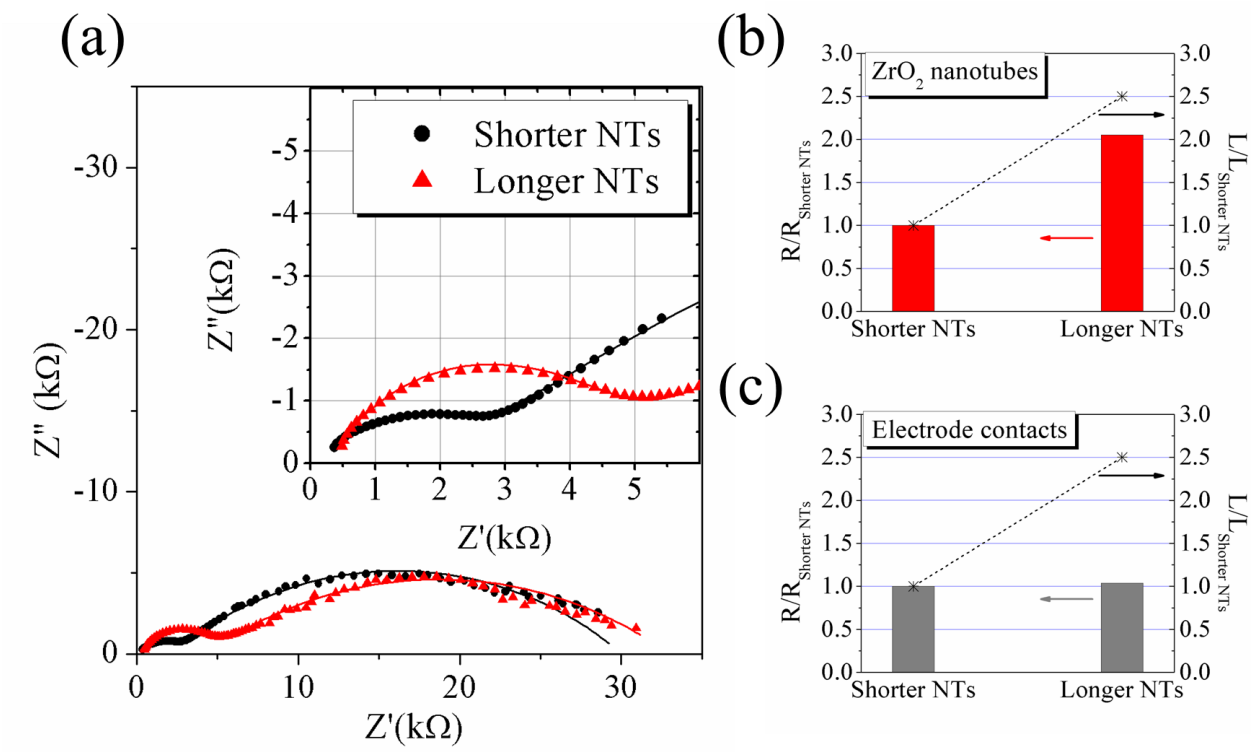

Figure 7. (a) Impedance spectra, obtained from two ZrO_2 nanotubular films with different NT lengths at 600 ℃ in N_2. The bar graphs show the effect of ZrO_2 NT thickness on (b) the resistance of the ZrO_2 NTs and (c) on the contact resistance.

The impedance spectroscopy results obtained at different temperatures and their corresponding fits to the circuit (Figure 6b) are shown in Figure 8. Very good fittings are obtained, with two impedance arcs seen at each temperature. The decreasing total resistance with increasing temperature is consistent with a thermally activated process dominating the impedance. Although both impedance arcs shrink in size with increasing temperature, it is evident that, at lower temperatures, the magnitude of the high frequency arc is larger than that of

the low frequency process, while the low frequency process starts to dominate the overall impedance response as the temperature increases.

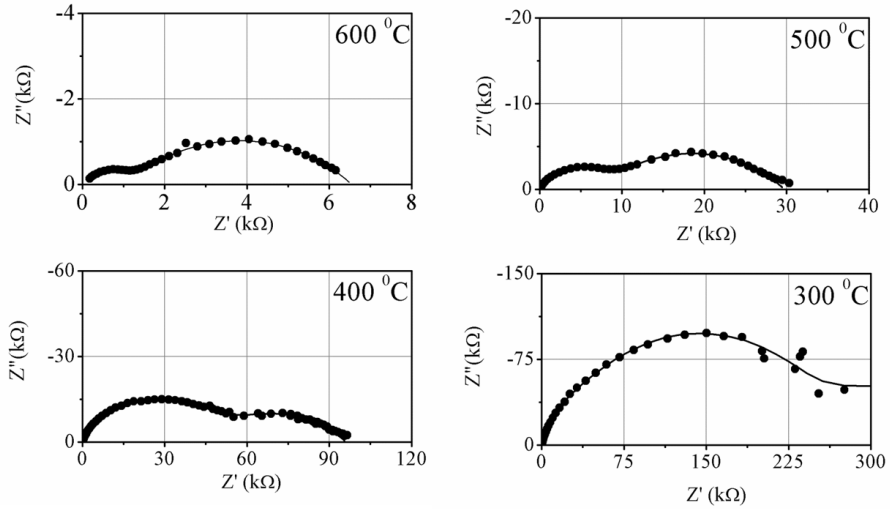

Figure 8. Impedance spectra obtained for 2 μm thick ZrO_2 nanotubular film at various temperatures in N_2.

Figure 9 provides the temperature dependence of the area specific resistances (ASR), calculated for each arc ($ASR_{contact}$ at low frequencies and ASR_{ZrO2} at high frequencies) using the following formulae:

$$ASR_{contact} = R_{contact} \times A \text{ and } ASR_{ZrO2} = R_{ZrO2} \times A \quad (1)$$

where

$$R_{contact} = R2 \text{ and } R_{ZrO2} = R1 \quad (2)$$

and "A" refers to the contact area between the Ag current collector material and the outer surface of the ZrO_2 nanotubular array. ASR_{ZrO2} represents a thermally activated process with an activation energy of 0.45 eV in the temperature range of 300-450 ℃. At higher temperatures (450-600 ℃), ASR_{ZrO2} starts to exhibit a stronger temperature dependence, with an activation energy of 0.90 eV. Eder et al. has also observed two electrical conduction regimes in nanocrystalline ZrO_2 samples [35]. The lower activation energy was ascribed to the formation of defects at the surface, while the higher activation energy was related to the electrical conduction dominated by electrical transport in the bulk ZrO_2 [35].

Although there is consensus in the literature that a significant part of the electrical conductivity of undoped ZrO_2 is related to electronic conductivity, the relatively high open circuit potential of 0.91 V obtained in a μ-SOFC utilizing an undoped ZrO_2 electrolyte (30-50 nm in thickness) by Ko et al, suggests that ZrO_2 possesses substantial ionic conductivity as well at these temperatures [15]. Nasrallah et al. attempted to differentiate the ionic and electronic contributions to the total electrical conductivity in doped and undoped ZrO_2 [36]. It was reported that, although electronic conduction is dominant, in general, a strong temperature and oxygen partial pressure dependence of the transference number (ratio of ionic conductivity to total electrical conductivity) was observed. For example, at oxygen partial pressures of 10^{-12} atm, the transference number was 0.1 at 600 ℃, while at oxygen partial pressures between 10^{-3} and 0.21 atm, the transference number was as high as 0.4. In addition, it was reported that the transference number increased with decreasing temperature [36], which is beneficial for μ-SOFCs that operate at temperatures below 600 ℃. From another perspective, Kerman et al determined that yttria stabilized zirconia electrolytes would approach their dielectric strength limit at a thickness of 6 nm and then begin to exhibit electronic leakage [37]. Although it was acknowledged that the

electronic leakage would decrease the open circuit potential, it was also mentioned that, at sufficiently high leakage rates, this can result in higher power densities due to the overall higher total current density passed. [37].

It is also worth noting that, with increasing temperature, ASR_{ZrO2} decreases more rapidly than does $ASR_{contact.}$ This results in the domination of the overall resistance by $ASR_{contact}$ at temperatures above 400 ℃. Therefore, by using impedance spectroscopy instead of dc methods to determine NT resistivity, which was shown here to allow the separation of the ZrO_2 and contact resistances, significant errors were avoided. For example, at 600 ℃, a total area specific resistance of 750 $\Omega.cm^2$ would have been measured by dc methods, while impedance spectroscopy allowed us to determine that only 150 $\Omega.cm^2$ of this resistance is due to the ZrO_2 NTs. The relatively high contact (electrode) resistances, observed here, should be lowered in order to obtain high power densities in a μ-SOFC device. This could be achieved when materials with good electrocatalytic properties (e.g., Ni and Pt for the anode and cathode, respectively) are infiltrated into the NTs to serve as the μ-SOFC electrodes.

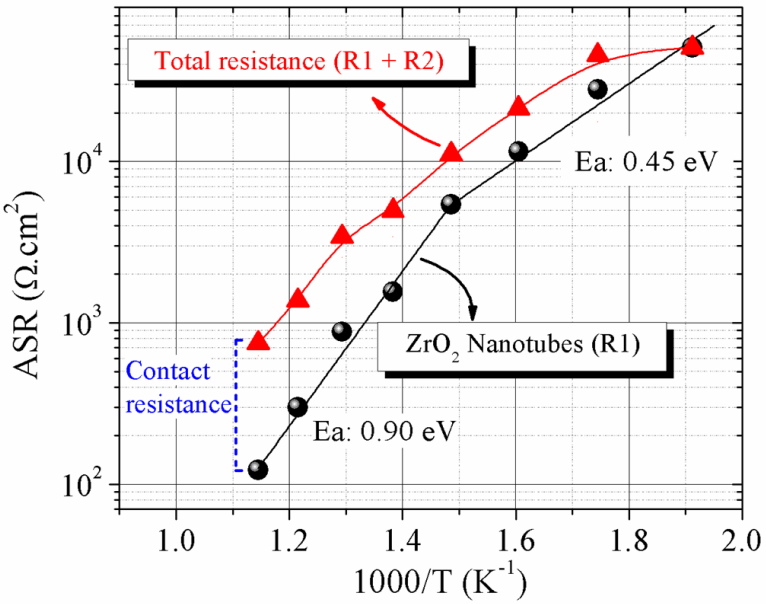

Figure 9. Temperature dependence of the area specific resistance (R1 in Figure 6b) of 2 μm thick ZrO_2 nanotubular film and the total area specific resistance (ZrO_2 NTs + contact resistance) in a N_2 environment.

The electrical conductivity (σ) of the ZrO_2 nanotubular films was then calculated from the R1 values obtained from impedance spectroscopy (Figure 8), using Equation (3),

$$\sigma = (1/R) \times (L/A) \quad (3)$$

where "L" refers to the ZrO_2 NT length (film thickness) and "A" the Ag/ZrO_2 contact area. The electrical conductivity values, calculated for each temperature, are given in Figure 10. Data obtained by Petrovsky et al. from in-plane DC conductivity measurements of ZrO_2 thin films on sapphire substrates, in air [38], are also shown in the plot for comparison, as well as the electrical conductivity values reported by Eder et al., for the impedance of nanostructured ZrO_2 in H_2 [35]. The similarity of these temperature dependence trends validates the approach used here,

especially the selection of R1 (high frequency resistance) as representing the resistance of the ZrO_2 NTs.

The ZrO_2 nanotubular films exhibit an electrical conductivity of 1.8×10^{-6} S/cm at 600 ℃, which is almost twice the value obtained by Petrovsky et al. at this temperature for dense ZrO_2 thin films [38]. In fact, the ZrO_2 film porosity of ~ 16 % should have lowered the overall conductivity, not increased it. Although it is possible that the higher electrical conductivity obtained here is due to the more reducing atmosphere used in the present work, when used in the μ-SOFC application, the ZrO_2 NTs will be subjected to even more reducing atmospheres at the anode side in the presence of hydrogen fuel, as well as a more oxidizing one at the cathode side, in air. Therefore, it is reasonable to assume that the electrical conductivity values obtained here in N_2 are a good representation of the electrical conductivity that the ZrO_2 NTs will exhibit. It is also possible that fluoride ions, incorporated into the ZrO_2 NTs (see EDX results in Figure 4), have created additional point defects, which could enhance the electrical conductivity. However, it has also been reported by others that fluoride is almost completely removed from the anodically formed ZrO_2 NTs after heat treatment at 300 ℃ for 6 hours [39]. Since the electrical measurements were carried out only after annealing at 600 ℃ in the present work, it can be concluded that no fluoride ions would still be present in the nanotubular film structure and thus that these impurity species could not have had any influence on the measured conductivity of the films.

Another possible explanation for the higher electrical conductivity exhibited by the ZrO_2 nanotubular films investigated here (Figure 10) is their high surface area to volume ratio, which could facilitate electrical conduction along the NT surfaces where the defect concentrations are

high [35]. To test this hypothesis, further experiments involving the effect of NT inner diameter on the measured resistance are currently underway.

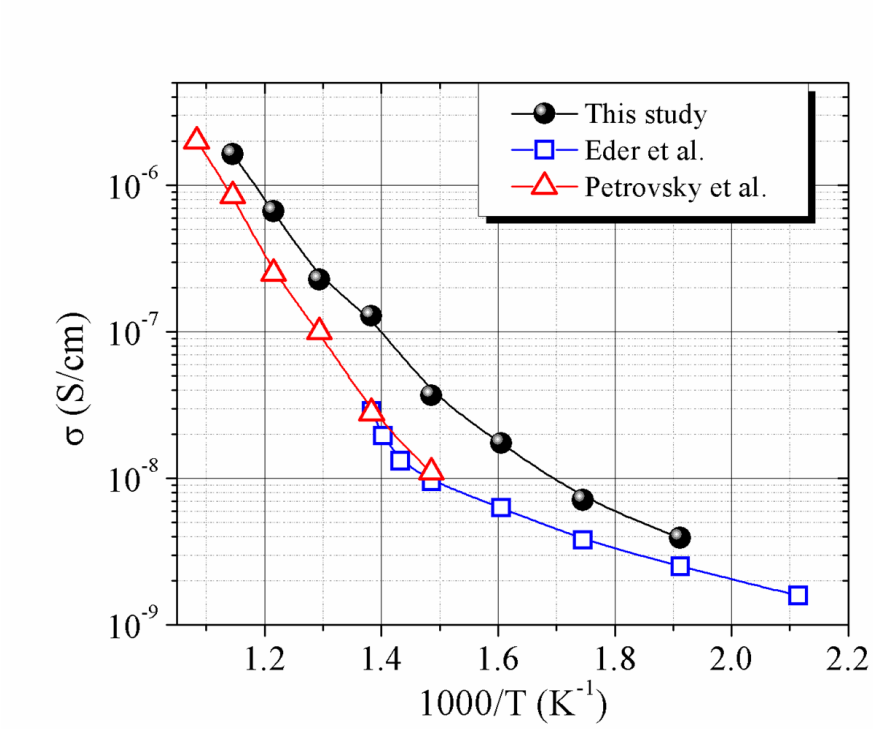

Figure 10. Temperature dependence of electrical conductivity of 2 μm thick ZrO_2 nanotubular films compared with conductivity values from the literature for dense ZrO_2 ceramics and thin films.

Conclusions

Recent studies have shown that micro solid oxide fuel cells (μ-SOFCs), utilizing undoped ZrO_2 thin films as the electrolyte, can yield good open circuit potentials (OCPs) and respectable power densities. Therefore, in this work, anodically grown ZrO_2 nanotubular films are examined as structures to further improve the power densities of these devices. It is suggested that, upon electrocatalyst infiltration into the NTs, the ZrO_2 NT base (15-25 nm thickness) could serve as

the ultra-thin electrolyte and the triple phase boundary (TPB) length would be significantly extended by utilizing the electrocatalyst/ZrO_2 interface on the NT walls as the active reaction sites. To realize this objective, the electrical characteristics of the ZrO_2 nanotubular films must first be known.

In this work, robust ZrO_2 nanotubular films were fabricated by anodization and the electrical conductivity of the nanotubular arrays was determined by impedance spectroscopy. The ZrO_2 nanotubular films were fabricated for the first time using a two-step anodization process. This resulted in crack-free ZrO_2 nanotubular films that adhered strongly to the Zr metal substrate, which was required for accurate electrical evaluation of the NTs.

Impedance spectroscopy measurements were then carried out, as this approach can separate the electrode contact resistance from the ZrO_2 nanotubular film resistance. This, in turn, allowed the accurate determination of the electrical conductivity of the ZrO_2 nanotubular films, shown here to be approximately two times higher than what was reported in prior literature for ZrO_2 ceramics and thin films. The activation energy for the electrical conductivity of ZrO_2 NTs was determined to be 0.45 eV in the temperature range of 250-400 ℃ and 0.90 eV in the temperature range of 400-600 ℃, which is consistent with earlier reports. The very good electrical conductivity values obtained here can be used to project a power density of 100-200 mW/cm^2 at 600 ℃, which supports the further development of μ-SOFCs utilizing ZrO_2 NTs as the electrolyte and the electrocatalytic layers.

Acknowledgements

The authors gratefully acknowledge the Eyes High PDF Program at the University of Calgary and Alberta Innovates – Technology Futures (AITF) for the support of AB, as well as the Natural Sciences and Engineering Research Council of Canada (NSERC) for the overall financial support of this work.

References

1. P. Roy, S. Berger and P. Schmuki, *Angewandte Chimie*, 2011, **50,** 2904.
2. A. L. Linsebigler, G. Lu and J. T. Yates, *Chemical Review*, 1995, **95**, 735.
3. S. Y. Huang, L. Kavan, I. Exnar and M. Graetzel, *Journal of the Electrochemical Society*, 1995, **142**, L142.
4. A. Ghicov and P. Schmuki, *Chemical Communications*, 2009, **20**, 2791.
5. G. Zhang, H. Huang, Yihe Zhang, H. L. W. Chan and L. Zhou, *Electrochemistry Communications*, 2007, **9**, 2854.
6. D. Yang, H. Kim and S. Cho, W. Choi, *Materials Letters*, 2008, **62,** 775.
7. S. Sreekantan, R. Hazan and Z.Lockman, *Thin Solid Films*, 2009, **518**, 16.
8. M. Paulose, K. Shankar, S. Yoriya, H. E. Prakasam, O. K. Varghese, G. K. Mor, T. A. Latempa, A. Fitzgerald, and C. A. Grimes, *Journal of Physical Chemistry B*, 2006, **110**, 16179.
9. W. Lee and W. H. Smyrl, *Electrochemical and Solid-State Letters*, 2005, **8,** B7.
10. L. Li, D. Yan, J. Lei, J. He, S. Wu, F. Pan, *Materials Letters*, 2011, **65**, 1434.

11. N. Q. Minh, *Journal of the American Ceramic Society*, 1993, **76**, 563.

12. V. V. Kharton, F. M. B. Marques and A. Atkinson, *Solid State Ionics*, 2004, **174**, 135.

13. J. W. Fergus, *Journal of Power Sources*, 2006, **162**, 30.

14. O. Yamamoto, *Electrochimica Acta*, 2000, **45**, 2423.

15. C. Ko, K. Kerman and S. Ramanathan, *Journal of Power Sources*, 2012, **213**, 343.

16. M. Motoyama, C. C. Chao, J. An , H. J. Jung, T. M. Gür , and F. B. Prinz, *ACS Nano*, 2014, **8**, 340.

17. H. Jha, R. Hahn, P. Schmuki, *Electrochimica Acta*, 2010, **55**, 8883.

18. C. Chen, H. Chung, C. Chen, H. Lu, C. Lan, S. Chen. L. Luo, C. Hung and E. W. Diau, *Journal of Physical Chemistry C*, 2008, **112**, 19151.

19. N. K. Allam, X. J. Feng and C. A. Grimes, *Chemistry of Materials*, 2008, **20**, 6477.

20. H. A. El-Sayed and V. I. Birss, *Nano Letters*, 2009, **9**, 1350.

21. A. Tighineau, T. Ruff, S. Albu, R. Hahn and P. Schmuki, Chemical Physics Letters, 2010, 494, 260.

22. C.E. Coleman, D. Hardie, *Journal of the Less Common Metals*, 1966, **11**, 168.

23. C.J. Simpson, C.E. Ells, *Journal of Nuclear Materials*, 1974, **52**, 289.

24. H. A. El-Sayed, H. M. Molero and V. I. Birss, *Nanotechnology*, 2012, **23**, 435602.

25. S. Singh, W. R. T. Barden and P. Kruse, *ACS Nano*, 2008, **2**, 2453.

26. H. A. El-Sayed and V. I. Birss, *Journal of Materials Chemistry*, 2011, **21**, 18431.

27. S. Li, G. Zhang, D. Guo, L. Yu and W. Zhang, *Journal of Physical Chemistry C*, 2009, **113**, 12759.

28. L. Li, Z. Zhou, J. Lei, J. He, S. Wu and F. Pan, *Materials Letters*, 2012, **68**, 290.

29. D. Yu, Y. Song, X. Zhu, C. Yang, B. Yang and H. Xiao, *Materials Letters*, 2013, **109**, 211.

30. D. Fang, K. Huang, Z. Luo, Y. Wang, S. Liu and Q. Zhang, *Journal of Materials Chemistry*, 2011, **21**, 4989.

31. T. H. Choudhury, M. Rajamathi and S. Raghavan, *Journal of Materials Chemistry*, 2012, **22**, 6885.

32. P. Jasinski, V. Petrovsky, T. Suzuki, T. Petrovsky and H. U. Anderson, *Journal of the Electrochemical Society*, 2005, **152**, A454.

33. Q. Li and V. Thangadurai, Fuel Cells, 2009, **9,** 684.

34. B. Butz, P. Kruse, H. Störmer, D. Gerthsen, A. Müller, A. Weber and E. Ivers-Tiffée, *Solid State Ionics*, 2006, **177**, 3275.

35. D. Eder and R. Kramer, *Physical Chemistry Chemical Physics*, 2006, **8**, 4476.

36. M. M. Nasrallah and D. L. Douglas, *Journal of the Electrochemical Society*, 1974, **121**, 255.

37. K. Kerman and S. Ramanathan, *Journal of Applied Physics*, 2014, **115**, 174307.

38. T. Petrovsky, H. U. Anderson and V. Petrovsky, Materials Research Society Proceedings, ed. P. Knauth, J-M. Tarascon, E. Traversa, H.L. Tuller, Materials Research Society, 2002, pp. 515 – 520.

39. W. J. Lee and W. H. Smyrl, *Current Applied Physics*, 2008, **8**, 818.